

Crystallization of 8 mol% yttria-stabilized zirconia thin-films deposited by RF-sputtering

R. Frison ^{a,*}, S. Heiroth ^b, J.L.M. Rupp ^c, K. Conder ^a, E.J. Barthazy ^d, E. Müller ^d, M. Horisberger ^a, M. Döbeli ^e, L.J. Gauckler ^{f,g}

^a Laboratory for Development and Methods, Paul Scherrer Institut, 5232 Villigen-PSI, Switzerland

^b General Energy Research Department, Paul Scherrer Institut, 5232 Villigen-PSI, Switzerland

^c Massachusetts Institute of Technology (MIT), Department of Materials Science and Engineering and Department of Nuclear Science and Engineering, 77 Massachusetts Ave, Cambridge, MA 02139, USA

^d Electron Microscopy ETH Zurich (EMEZ), ETH Zurich, Wolfgang Pauli Str. 16, 8093 Zurich, Switzerland

^e Ion Beam Physics, ETH Zurich, 8093 Zurich, Switzerland

^f Nonmetallic Inorganic Materials, Department of Materials, ETH Zurich, Wolfgang Pauli Str. 10, 8093 Zurich, Switzerland

^g International Institute for Carbon Neutral Energy Research (WPI-I2CNER), Kyushu University, 744 Moto-oka, Nishi-ku, Fukuoka 819-0395, Japan

ARTICLE INFO

Article history:

Received 14 May 2012

Received in revised form 1 October 2012

Accepted 12 November 2012

Available online 23 December 2012

Keywords:

Crystallization

Grain growth

Thin films

Ceramics

Yttria stabilized-zirconia

RF-sputtering

ABSTRACT

The crystallization upon thermal treatment of 8 mol% yttria-stabilized zirconia thin films deposited by RF-sputtering at room temperature is investigated. The as-deposited YSZ films are biphasic with crystallites of 5–10 nm in diameter building a columnar-like microstructure. Fully crystalline YSZ thin films are obtained after isothermal dwells in the temperature range 800–1100 °C. X-ray diffraction and Raman spectroscopy demonstrate that the crystalline films have a cubic structure retained even after high-temperature annealing while a strong texture is developed. Further, a stagnating grain-growth is observed, characterized by a final grain size of about 60 nm and a micro-strain of 0.15%. Given the observed films' micro-structural stability, their application in miniaturized electrochemical devices such as micro-solid oxide fuel cells or sensors can be foreseen.

© 2012 Elsevier B.V. All rights reserved.

1. Introduction

In the last years the use of thin films in micro solid oxide fuel cells (SOFC) [1,2] or chemical sensors [3,4] allowed to reduce their size and operating temperature [5,6]. Yttria stabilized zirconia is used as electrolyte membrane in micro solid oxide fuel cells with thicknesses of some hundred of nanometers [7–9]. YSZ thin films can be produced by physical vapor deposition techniques, including sputtering and pulsed laser deposition, as well as by chemical and liquid precursor precipitation methods like chemical vapour deposition, sol-gel, spin- or dip-coating and spray pyrolysis [7,10]. Depending on the thin films' deposition temperature crystalline [11,12], biphasic [7] or amorphous films [13,14] are obtained. Amorphous and biphasic thin films are then crystallized by a post deposition annealing process in order to tailor the thin films' properties. The microstructural characteristics affect the electrical [15,16], optical [17,18] and mechanical [9,17,19] properties of the thin films. Literature data of the total conductivity of YSZ thin films differ more than two orders of magnitude [15,16,20].

Such scatter may primarily originate from differences in degrees of crystallinity, strain or phase composition [21–23].

Knowledge of the crystallization and grain growth processes is therefore at the basis of microstructural engineering essential for the production of electroceramic components with desired properties. Despite their technological importance, the crystallization and grain growth of ceramic metal oxide thin films have been only studied in few cases [13,24–26]. Recently time-temperature-transformation (TTT) diagrams have been proposed for ceria-based thin films to describe the degree of crystallinity over time and temperature relative to the films' deposition conditions [25]. In case of sputter deposition, many studies were dedicated to the role of Y-doping level on the crystal structure of the thin films [27–30], or to the deposition conditions on the elemental composition [31,32]; no study focused on the crystallization of YSZ thin films.

In this work, we study the thermal stability of the amorphous state along with the kinetics of crystallization and grain growth of 8 mol%-YSZ thin films deposited by radio frequency sputtering at low temperature. The results will clarify whether YSZ-thin films processed by low temperature sputtering develop a stable microstructure and will help to optimize the thin films' properties for their use in micro-solid oxide fuel cells.

* Corresponding author.

E-mail address: ruggero.frison@gmail.com (R. Frison).

2. Experimental

Yttria-stabilized zirconia (YSZ) thin films were deposited on c-cut sapphire single crystal substrates ($10 \times 10 \times 0.5$ mm, <0001>, $a_{\text{Al}_2\text{O}_3} = 4.763$ Å and $c_{\text{Al}_2\text{O}_3} = 13.003$ Å) by RF-sputtering technique using an Advanced Energy Cesar 1.36 generator operating at 13.56 MHz coupled with a 25.4 mm Angstrom circular magnetron mounted on a standard DN 400 KF recipient. Commercial YSZ powders, 8 mol% Y_2O_3 99.9% purity TOSOH Inc. Japan, were pressed into pellets and air-sintered at 1600 °C for 10 h in order to obtain a dense target of 25.4 mm diameter. Before each process the deposition chamber was pumped down to 2×10^{-6} mbar, while during deposition a pressure of 8×10^{-3} mbar was obtained introducing Ar and O_2 in the ratio $p_{\text{O}_2}/p_{\text{Ar}} = 0.2$. The RF-power was fixed to be 40 W which, with a target-substrate distance of 80 mm, allowed a deposition rate of 2 nm/min. The substrate temperature during deposition was 120 °C as recorded by a thermocouple embedded in the sample holder stage.

The film thicknesses were analyzed by surface profilometry and scanning electron microscopy (SEM) using a Dektak 8 system and a Zeiss Supra VP55, respectively. Grain size distributions were obtained from top view scanning electron microscopy (SEM) images by the Heyn's mean lineal intercept method [33], measuring at least 500 individual grains. Rutherford backscattering spectroscopy (RBS) and particle-induced X-ray emission (PIXE) using 2 MeV ^4He ions and 3 MeV protons as projectiles provided information on the chemical composition of the films.

In order to study the crystallization of the 8 mol%-YSZ thin films, the as-deposited samples were annealed in air at different temperatures between 800 and 1100 °C for dwell times from 1 min to 85 h. The as-deposited and annealed samples were analyzed with X-ray diffraction (XRD) using a Bruker D8 Advance diffractometer with a Copper anode and a Ni-filter. For the analysis of the crystallinity, because of the limited number of diffraction peaks and the strong texture observed, only (220) peak of the YSZ film was fitted with a pseudo-Voigt function using the FIT software [34], from which the integrated peak area $A(\theta)$ and the integral breadth $\beta(\theta)$ of the peak were determined. The volume weighted average diameter of crystalline grains D and microstrain ε were determined from the integral breadths of the Lorentzian and Gaussian components of the pseudo-Voigt function, respectively β_L and β_G , as described in Ref. [35]:

$$D = \frac{K_\beta \lambda}{\beta_L \cos(\theta)} \quad (1)$$

$$\varepsilon = \frac{\beta_G}{4 \tan(\theta)} \quad (2)$$

where K_β is the Scherrer constant, which for ($hh0$) reflexes and cubic shape is $3/(2\sqrt{2})$ [36].

Transmission Electron Microscopy (TEM) analyses were performed on specimens prepared by the classical cross-section technique, with the thickness reduced to electron transparency by ion-etching using Ar gas (4.3 kV acceleration voltage, 4° etching angle of the beam relative to the surface). Conventional bright field images were acquired using a Philips CM30ST and a FEI Tecnai F30 FEG transmission electron microscope (300 keV, point to point resolution: ~0.2 nm).

Additional information about the film phase composition was obtained by Raman spectroscopy employing a confocal Raman microscope (LabRAM Series, Horiba Jobin Yvon) with a He–Ne excitation laser ($\lambda = 632.8$ nm, output power ~10 mW) focused to probe an analyte volume of ~1 μm^3 . The YSZ thin films measured by Raman spectroscopy were deposited on 5.0 mm \times 5.0 mm \times 0.5 mm LaAlO_3 (100) crystalline substrates ($a_{\text{LaAlO}_3} = 3.821$ Å), as described above. The choice of different substrates was necessary in order to avoid the superposition of film's and substrate's Raman peaks.

3. Results and discussion

3.1. Thin film morphology

The as-deposited films, 200 ± 10 nm thick, showed a good adhesion to the sapphire substrate with homogeneous and dense microstructure as revealed by SEM analyses, (see Fig. 1).

Additionally, SEM cross section-images revealed a tendency to develop a columnar microstructure, as it is represented in Fig. 1. Typical column width ranged from 20 to 40 nm.

High resolution TEM micrographs of as-deposited samples, Fig. 2, confirmed SEM results and, additionally, revealed the formation of a biphasic polycrystalline structure with small crystallites (dark spots) of size from 5 to 10 nm, dispersed into a low-contrast matrix which could be attributed to crystallites out of Bragg condition (respect to the electron beam direction) or to amorphous material. This is a typical effect observed in a polycrystalline material deposited at low temperature [37]. We conclude that a biphasic amorphous-crystalline microstructure for the as-deposited film was obtained. The crystallites, starting from the initial nucleation centers, grow along a preferential direction with the grain boundaries oriented vertically building up an array of rod-shaped columns each surrounded by lower density material. In TEM micrographs of 500 °C-annealed samples, shown in Fig. 3, an increase of crystallized phase volume with respect to the as-deposited sample (Fig. 2) could be qualitatively estimated by observing the density of the dark spots and the columnar alignment. Further, after a close inspection of the TEM micrographs (Figs. 2 and 3), presence of pores could be excluded as, if present, they would appear as light spots within the sample matrix. Additional scanning TEM pictures were acquired confirming such conclusion.

3.2. Thin film structure

The results obtained from the TEM analyses were confirmed by the results of the XRD experiments as shown in Fig. 4, where a comparison of diffraction pattern of the as-deposited and ex-situ annealed samples is presented. In the case of the as-deposited samples (lowest panel) the diffraction pattern clearly showed a distinct though very broadened Bragg peak, typical of small crystallites and lattice defects [38]. The diffraction patterns, Fig. 4, matched both the reference patterns of the cubic: ICDD PDF-card #01-030-1468 and tetragonal: ICDD PDF-card # 01-070-4432 phases of 8 mol%-YSZ though with a significant peak shift of $\Delta 2\theta_{(200)} \sim 0.15^\circ$. The thermal treatment in air led to the crystallization of the films. Fig. 4 presents the diffraction patterns of 8 mol%-YSZ thin films ex-situ annealed at different temperatures for 20 h, where the characteristic peaks of YSZ could be observed. The comparison of the diffraction pattern clearly revealed a systematic shift to larger Bragg angles of the peak maxima with increasing annealing temperature. Additionally the diffraction peaks became progressively sharper and more intense indicating a simultaneous increase of the crystallized fraction and domain size. Further, a strong (220) preferential orientation developed. A (220) preferential orientation differs from usual pulsed laser deposition and spray pyrolysis [13,26,39,40] where a (111) or (100) preferential orientation is generally observed. In case of sputter deposition, however, the (220) is observed when deposition conditions similar to the present were employed [18,41]. In a detailed study on ion beam assisted electron beam YSZ thin films deposition Sonnenberg *et al.* [42] established a correlation between growth direction and ion/atom ratio in the gas: at low values of ion/atom ratio (220), whereas at high values (111) developed. Thus, following Sonnenberg *et al.*, the present observations could be the result of a low ionization level of the plasma produced by the mild sputtering power applied, the relatively high deposition pressure and the atmosphere composition which favours the ions recombination. The topmost panel in Fig. 4 shows the XRD pattern of an 8 mol%-YSZ

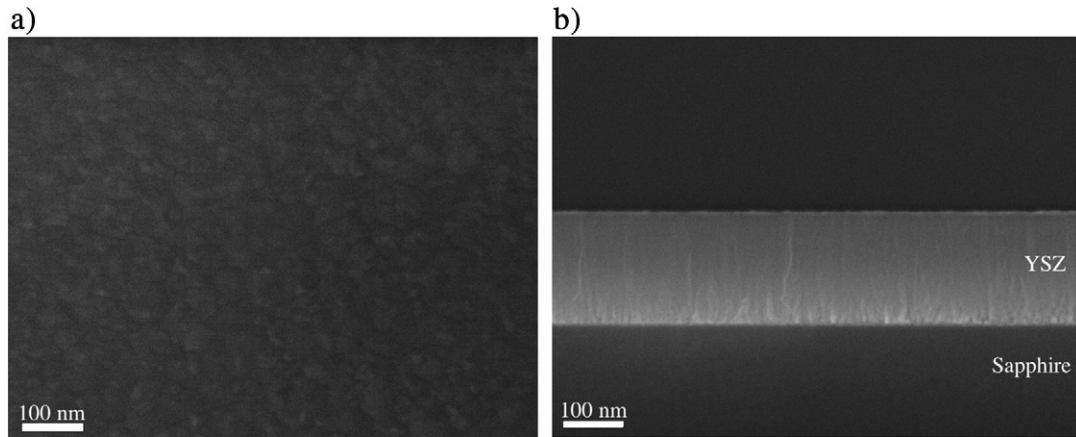


Fig. 1. SEM images: a) top view b) and cross section of ~200 nm thick as-deposited 8 mol%-YSZ thin film on sapphire substrate.

thin film ex-situ annealed at 1000 °C and deposited on a LaAlO_3 substrate. No significant change in the structural properties of the film could be observed compared to the thin films deposited on sapphire substrates.

Fig. 5 shows the Raman spectra of the RF-sputtering deposited 8 mol%-YSZ thin films annealed at different temperatures along with the spectra of an uncoated LaAlO_3 substrate.

The as-deposited sample presented a broad Raman signal at $\sim 618 \text{ cm}^{-1}$ with a shoulder at lower frequencies, while the Raman spectra of annealed samples showed a sharpening and shift towards higher wave numbers up to 630.0 cm^{-1} . The cubic phase of microcrystalline YSZ (c-YSZ) is characterized by only one active Raman mode for the F_{2g} stretching of the oxygen and cation ions, with reference position 617.2 cm^{-1} [45,46], while the tetragonal phase of YSZ (t-YSZ) by six distinctive Raman modes [43,44], as it is summarized in Table 1. Thus the cubic phase of YSZ was obtained as the six additional peaks characteristic of the tetragonal phase were absent (see Fig. 5). The only observed Raman mode, with peak position ranging from 617.6 to 630.0 cm^{-1} , could be therefore associated to the unique F_{2g} mode of the cubic phase of YSZ (c-YSZ) [45,46]. For Y-concentration higher than 8.6 mol% Gao et al. [30] observed only the F_{2g} -mode of the cubic phase with a shift to its reference position inversely proportional to the Y-concentration. Thus, the cubic-tetragonal

phase boundary was approximately located at a Y-concentration of 8.6 mol%, very close to the value of 8.53 mol% found in this study.

This outcome, however, was found to differ substantially from recent results on 8 mol%-YSZ deposited by pulsed laser deposition [13] and spray pyrolysis [26] where the formation of a tetragonal phase of YSZ (t-YSZ) upon annealing of as-deposited amorphous YSZ thin films was reported. The origin of such different behavior could be ascribed to the interplay of a markedly distinct initial microstructures and thin films' stoichiometry. In the present case the YSZ-thin films were characterized by a biphasic microstructure with preferentially oriented columnar nano-grains, (see Figs. 2 and 3), and an oxygen deficient composition as a stoichiometry of $\text{Zr}_{0.841 \pm 0.004}\text{Y}_{0.159 \pm 0.004}\text{O}_{1.85 \pm 0.004}$ was found in the sample annealed at 1000 °C. Thus it could be reasonable to expect that, upon annealing, the systems evolved towards an energetically favored final state characterized by a different microstructure, microstrain, texture and possibly also crystallographic symmetry. As 8 mol%-YSZ is located at the borderline of cubic-tetragonal in the YSZ phase diagram [47] even relatively small differences in terms of stoichiometry and microstructure may drive the system upon thermal treatment towards markedly different final states. Position, width and shape of the Raman modes are generally modified by several factors like crystallinity [49], defects [50,51], stress [52], micro-strain and particle size [53]. Asymmetric and shifted Raman spectrum with tailing

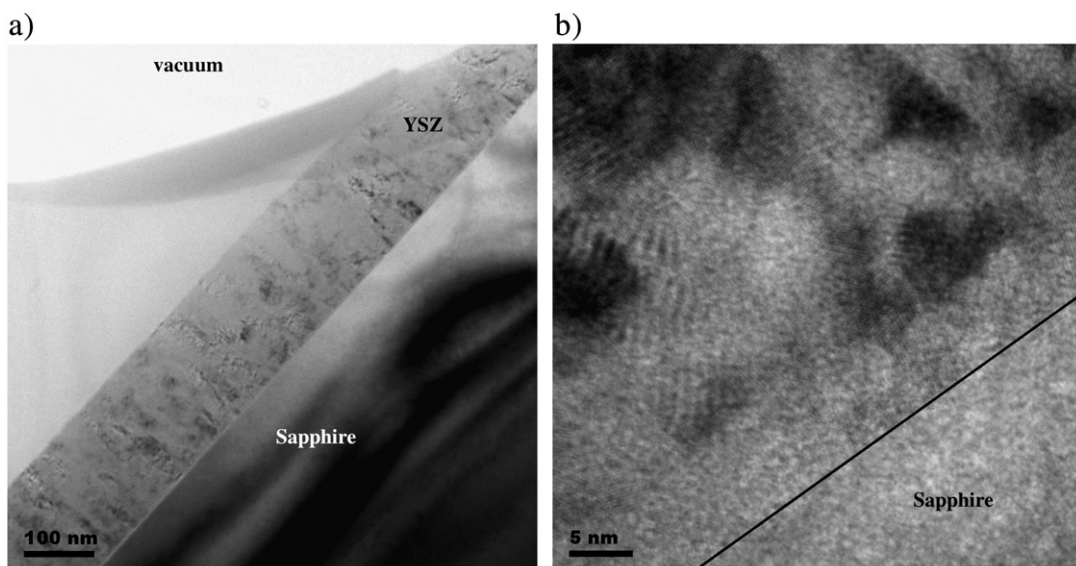


Fig. 2. TEM micrographs: a) cross section and b) detail of as-deposited 8 mol%-YSZ thin film on sapphire substrate.

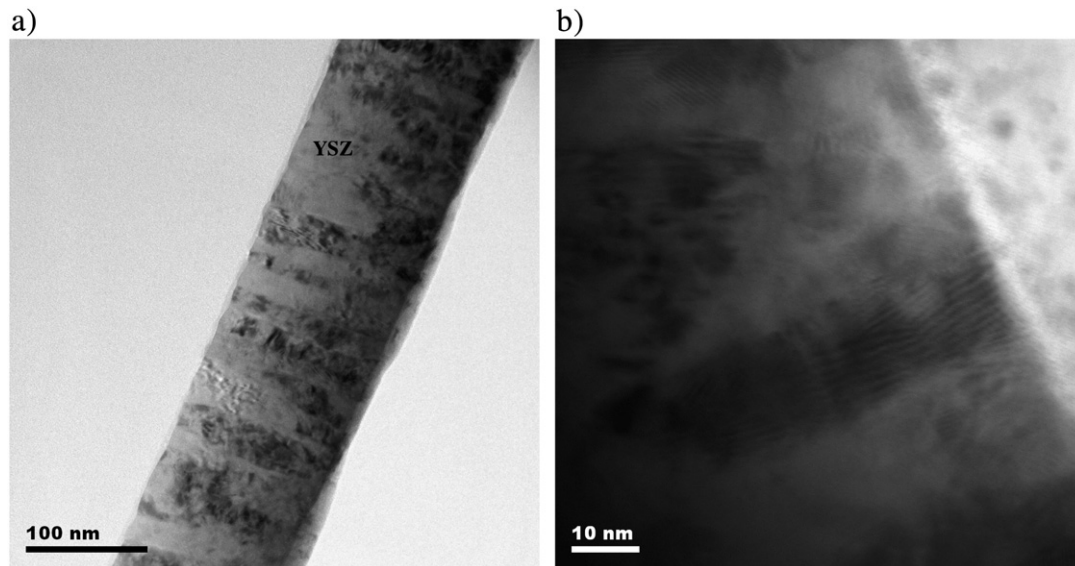


Fig. 3. TEM micrographs: a) cross section b) and detail of 8 mol%-YSZ thin film annealed at 500 °C for 20 h.

towards lower wave numbers has been observed and modeled in a number of studies on micro- and nano-crystalline materials like Si [54], CeO₂ [53] and TiO₂ [55]. In 8 mol%-YSZ powders a broad and asymmetric F_{2g} mode of the cubic phase with blue-shifts up to 8 cm⁻¹ was observed [56,57]. Such value reasonably compares with the maximum shift of 13 cm⁻¹ observed in this study, which could be well explained if additional contributions from strain and lattice contraction are assumed. Cai et al. [52], for instance, measured a blue shift of the F_{2g} mode up to 3 cm⁻¹ in 10 mol%-YSZ under uniaxial stress. Compressive stress may originate from difference in the thermal expansion coefficient of the substrate and the film ($\Delta\alpha \sim 1.0 \times 10^{-6} \text{ K}^{-1}$), or the relatively large difference between the lattice parameter of the substrate and YSZ thin film: being $a_{\text{LaAlO}_3} = 3.821 \text{ \AA}$ and $a_{\text{YSZ}} = 5.139 \text{ \AA}$, respectively.

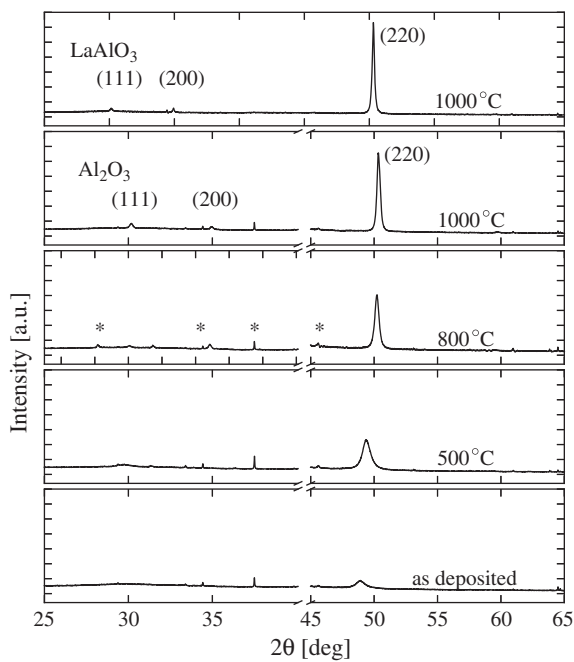


Fig. 4. XRD patterns of 8 mol%-YSZ thin films annealed at 1000, 800, 500 °C for 20 h and as-deposited. Asterisks (*) denotes contribution from the alumina substrate, 2θ-axis brake masks the (0001)-peak of Al₂O₃. In the topmost panel the XRD pattern of a 8 mol%-YSZ thin film deposited on LaAlO₃ substrate and annealed at 1000 °C is shown.

Generally, lattice defects, stress, limited domain size and micro-strain are often simultaneously present in nano-crystalline thin films, therefore for a precise estimation of their relative contribution to sputtered films of 8 mol%-YSZ under investigation further structural studies are required.

3.3. Crystallization and grain growth

The degree of crystallinity of the thin films, i.e. the transformed volume fraction during the crystallization process, was calculated as the ratio between the integrated peak area for the given annealing time, $A(t)$, and the reference value A_c of a complete crystallization obtained by annealing of 8 mol%-YSZ thin films at 1150 °C for 20 h

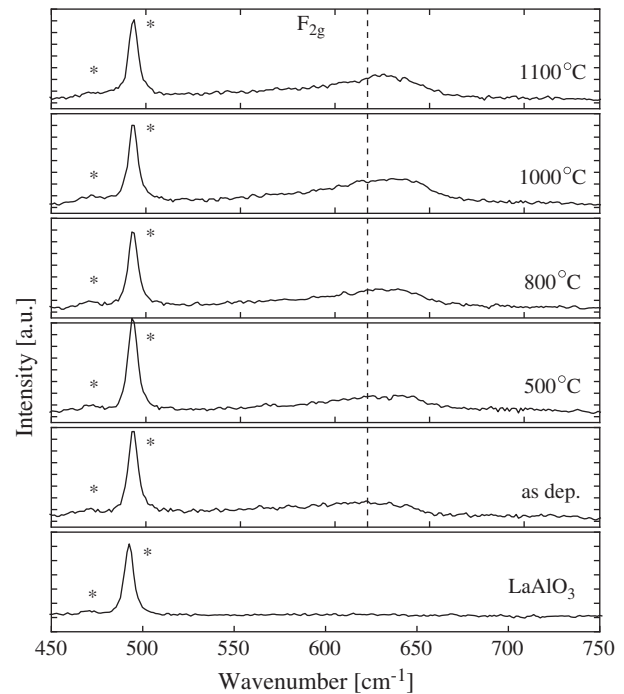


Fig. 5. Micro Raman spectra of, from bottom to up: uncoated LaAlO₃(100) substrate marked with asterisk (*), as-deposited and 500, 800, 1000, 1100 °C-annealed 8 mol%-YSZ films 1 μm thick. Spectra are background corrected for clarity. The vertical line marks the reference position of Raman bands in bulk cubic YSZ [43,44].

Table 1

Raman shifts, FWHMs and corresponding modes observed in YSZ powders of the cubic (c-YSZ) [45,46] and tetragonal (t-YSZ) [43,44] phases. LaAlO₃ is included for completeness.

Material	Raman shift	FWHM	Mode assignment	
	[cm ⁻¹]	[cm ⁻¹]	band	phase
LaAlO ₃ (100) YSZ	492.52	5.91	E _g	LAO [48]
	617.2	54.3	F _{2g}	c-YSZ
	256.5	30.3	E _g	t-YSZ
	318.2	29.8	B _{1g}	t-YSZ
	460.7	27.4	E _g	t-YSZ
	603.4	51.4	A _{1g}	t-YSZ
	640.0	23.8	E _g	t-YSZ

[58]: $X(t) = A(t)/A_c$. In Fig. 6 the evolution of the (220) peak on the annealing time at 1100 °C and the calculated crystallized fraction for two different temperatures are presented. As expected, the crystallization process progressed slower at the lower temperature – 800 °C – and required up to 40 hours to be accomplished, whereas at 1100 °C the crystallization could be fulfilled within 10 hours. The crystallization was accompanied by a lattice contraction as witnessed by the unit cell length reduction from 5.2523 Å to 5.125 Å corresponding to the as-deposited and annealed at 1000 °C for 20 h, respectively. Such contraction, however, should account also for a compressive stress component originating from the lattice misfit between the substrate and the YSZ thin films.

The isothermal grain growth at different temperatures is presented in Fig. 7, where the average apparent grain size was determined

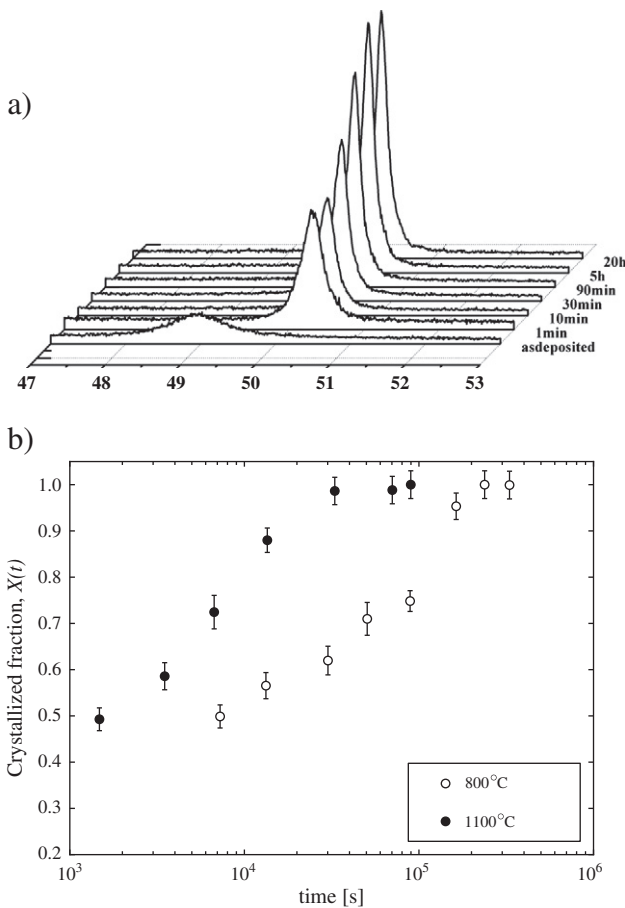


Fig. 6. a) evolution of the (220) peak on the annealing time at 1100 °C in 8 mol%-YSZ thin films. b) normalized volume fraction $X(t)$ of crystallized 8 mol%-YSZ thin films at 800 and 1100 °C.

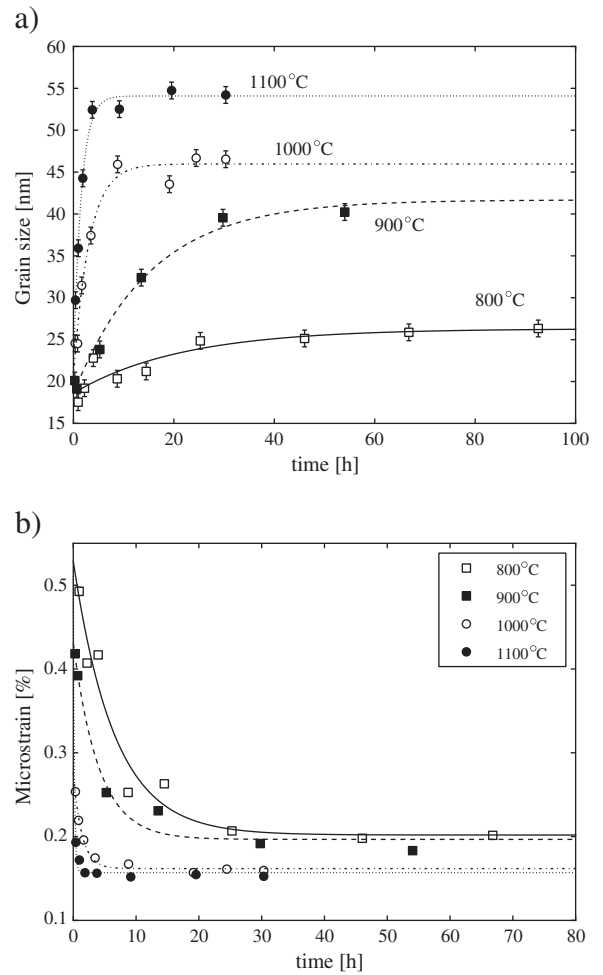


Fig. 7. a) Average grain size (markers) in 8 mol%-YSZ thin films as derived from XRD and least square fits (lines) according to Eq. (3); b) microstrain (markers) in 8 mol%-YSZ thin films as derived from XRD and least square fits (lines) according to Eq. (4).

applying the Scherrer equation (Eq. (1)) to the (220) peak. For each of the isothermal dwells the grain growth occurs mostly during an initial time period the length of which depends on temperature. Once such time is reached the grain growth slows down towards its apparent limiting value, which is temperature dependent and e.g. reaches 55 nm at 1100 °C; thus well below the sample thickness (200 nm). The average grain sizes here obtained were consistent with results on Ytria-doped Zirconia powders reported in the literature: Shi et al. [59] studied the isothermal crystallite growth of cubic and tetragonal YSZ reporting a grain size below 30 nm at 800 °C and of ~50 nm at 1000 °C, while above 1100 °C observed an increase in the growth rates which was attributed to the onset of a grain-boundary migration kinetics.

In Fig. 8 SEM micrographs of a 8 mol%-YSZ thin film annealed at 1100 °C is shown, while in Fig. 9 a grain size distribution as derived applying the Heyn's mean lineal intercept method [33]. The average grain size derived from the SEM images and XRD data showed a scatter in the case of the sample annealed at 1100 °C. Comparing the results, however, should bear in mind that the Scherrer equation refers the size of a coherently diffracting domain, which is not necessarily the same as the grain size. The analysis of the crystallite shape anisotropy requires the use of Williamson-Hall plot [38] or polar plots [60,61] which could not be employed on the basis of the diffraction patterns obtained.

Self-limited grain growth was described, according to Rupp et al. [62], by a relaxation function describing the average grain size $G(t)$

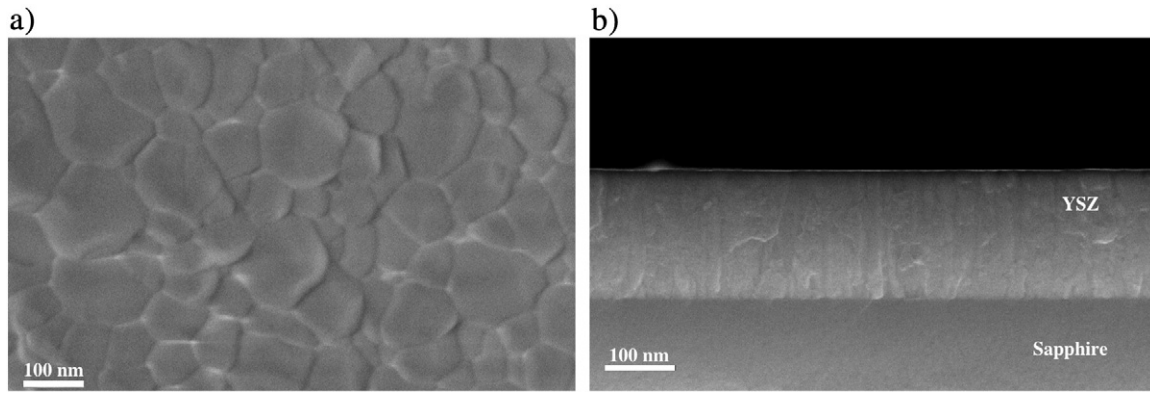


Fig. 8. SEM images: a) top view and b) cross section of 8 mol%-YSZ thin film annealed at 1100°C for 20 h deposited on Sapphire substrate.

characterized by a relaxation time t_G , a limited grain size G_1 , the initial grain size G_i and time t :

$$G(t) - G_i = (G_1 - G_i) \left[1 - \exp\left(-\frac{t}{t_G}\right) \right] \quad (3)$$

Grain growth stagnation in thin films was typically reported for solution based deposition techniques, like spray pyrolysis-deposited CeO_2 [62–64] or 8 mol%-YSZ deposited by spray pyrolysis [26] and spin-coating [65]. Similarly, Ji and coworkers [27] obtained by reactive RF-sputtering deposition an average grain size of 45 nm at 1000 °C. Further, a grain growth stagnation was reported by Gorman et al. [66] for unsupported porous YSZ thin films deposited by spin-coating and by Theunissen et al. [67] YSZ prepared by sol-gel precipitation.

The grain growth stagnation was attributed to elastic strain in amorphous phase and carbon impurities [24,63] or solution drag and Y-cation segregation at grain boundaries [65].

Several effects are known to cause such a stagnation of the grain growth, e.g. secondary phases, solute drag, strain, grain size to film thickness ratio, or triple junctions [68,69]. Yan et al. attributed the observed stagnation to the presence of a secondary phase, like pores, which reduced the mobility of the grain boundaries [70], while Dong et al. to solution drag or Y-cation segregation at grain boundaries. Rupp et al. [24,63] found that the growth stagnation could be attributed to carbon impurities and elastic strain. Finally, Scherrer et al. [71] found that, similarly to Yan, the origin was in the high porosity of the thin

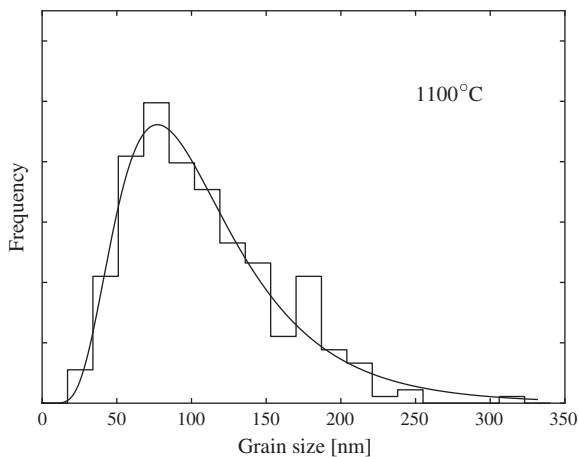


Fig. 9. Grain size distribution as derived from SEM intercept method in a 8 mol%-YSZ sample annealed at 1100 °C for 20 h. The solid lines represent least squares fits to a logarithmic normal function.

film prepared by spray-pyrolysis. It should be stressed, however, that most of the examples cited above refer to YSZ thin films deposited by precipitation based techniques where precursor residues and impurities are usually present. In the present case, instead, where the RF-sputtering deposition from a pure 8 mol%-YSZ target at high vacuum conditions provided a high level of purity of the samples (vide supra), such effect should be excluded. Thus, our experimental evidence suggests a strain effect, similarly to Ji [27] who obtained similar grain sizes in highly textured and strained YSZ thin films. A relatively large compressive stress may originate in the thermal treatment of the thin films. The thermal stress can be quantified by $\sigma = E(\alpha_{\text{sub}} - \alpha_{\text{film}}) \times (T_{\text{ann}} - T_m)$, where E is the Young modulus, α_{sub} and α_{film} the thermal expansion coefficient of the substrate and the film, respectively while T_{ann} and T_m the annealing temperature and the measurement temperature; thus, being $E > 0$ and $T_{\text{ann}} - T_m > 0$ while $\alpha_{\text{sub}} - \alpha_{\text{film}} < 0$ (since $\alpha_{\text{sub}} = 4.5 \times 10^{-6} \text{ K}^{-1}$ and $\alpha_{\text{film}} \approx 11 \times 10^{-6} \text{ K}^{-1}$), a large compressive strain can be generated. However, Scherrer et al. [71] observed, using STEM analyses, the formation of internal porosity after annealing samples at 800 °C and that this was larger than the porosity found at the film surface and at the interface with the substrate. In the present case, a similar effect cannot be excluded on the basis of the SEM surface analyses on high temperatures annealed and TEM analyses on as-deposited and 500 °C annealed samples. Thus we postpone additional investigations to clarify this point to a further study.

In Fig. 7b the evolution of microstrain is analyzed as a function of temperature and annealing time and compared to the grain growth data. Opposite to the grain growth case, the microstrain rapidly decreases within an initial time period after which a residual microstrain ε_L is reached. For the description of microstrain ε vs. t an exponential decay function was chosen:

$$\varepsilon = \varepsilon_L + \varepsilon_0 \exp\left(-\frac{t}{t_\varepsilon}\right) \quad (4)$$

where, similarly to Eq. (3) t_ε represents a relaxation time while ε_0 , ε_L the initial microstrain value and its residual value after relaxation, respectively.

The ε_0 and ε_L values determined in this work are in general lower than those reported in Refs. [26,62] for spray-pyrolyzed $\text{Ce}_{0.78}\text{Gd}_{0.22}\text{O}_{1.89}$ and 8 mol%-YSZ thin films. Such difference may be attributed to a higher concentration of impurities associated with the synthesis technique. The ε_L value at 1000 °C is $\sim 0.16\%$ and in a good agreement with literature values [13].

Increasing temperature leads to a decrease of the relaxation times for the grain growth kinetic as well as for the microstrain one. Microstrain and grain growth show relaxation times with a temperature dependent kinetic as shown in Fig. 10.

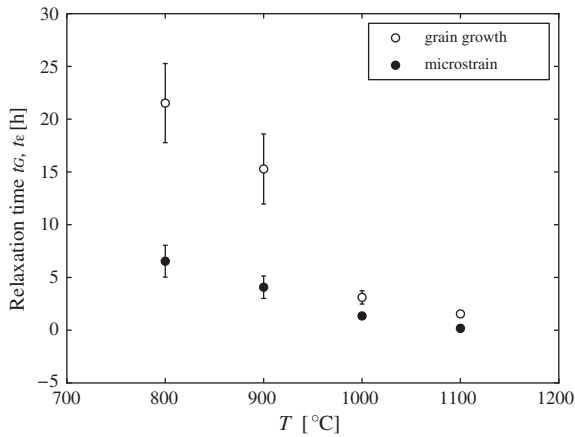


Fig. 10. Microstrain and grain growth relaxation time as a function of annealing temperature for 8 mol%-YSZ thin films.

The fit parameters obtained from Eq. (3) allowed to determine the chemical diffusivity D from [62]:

$$D = \frac{(G_1 - G_i)^2}{4\tau} \quad (5)$$

where G_1 , G_i have the meaning defined above and $\tau = t_C$ is interpreted as a chemical relaxation time. The temperature dependence of the diffusion coefficient could be fitted by an Arrhenius law with activation energy $E_a = 2.1 \pm 0.2$ eV (Fig. 11), indicating that in the temperature range under investigation the crystallization process occurred via a grain-boundary and interface diffusion. Such value for the activation energy close to the value of 1.3 eV obtained by Ramanathan et al. [72] in a study on the crystallization of 10 mol% YSZ gel prepared by precipitation methods. Similar studies based on Differential Scanning Calorimetry reported higher activation energies, from 2.4 to 3.5 eV [73,74].

The activation energy of Y- and Zr-diffusion in single crystalline YSZ, was measured by Kilo et al. [75] to be 4.2 and 4.5 eV respectively. It is well known, however, that grain boundaries represent lower energy pathways for atom movements and therefore it could be reasonable to expect a correspondingly lower activation energy in nano-crystalline systems where the contribution of the grain-boundary phase is relatively large. Drings et al. [76], for example, obtained an activation energy of 3 eV for Zr-diffusion at grain boundaries in sintered

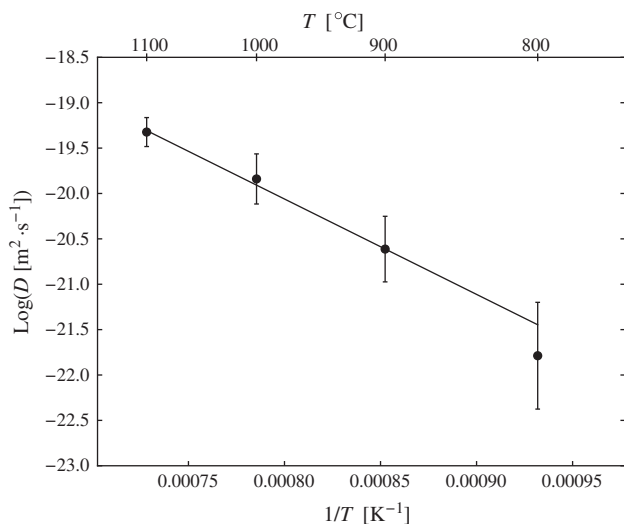


Fig. 11. Diffusion constant D as derived from fit of grain growth data with Eq. (3).

nano-crystalline YSZ by extrapolation from tracer diffusion secondary ion mass spectrometry data. In a recent detailed theoretical study on crystalline and amorphous YSZ Lau et al. [77] argued that in the amorphous metastable state the Zr^{4+} - and Y^{3+} -ions are as diffusive as the O^{2-} anions, for which of the activation energy was ~ 0.6 eV.

In contrast to present outcomes, Heiroth et al. [13] observed in pulsed laser deposited 8 mol%-YSZ thin films a grain growth ceasing only once the average grain size approached the film thickness. Such different behavior could be the result of the distinct initial microstructure. In the present case of sputtered 8 mol%-YSZ thin films the crystallization process starts from a biphasic system with already preferentially oriented columnar nano-grains whereas the as-deposited PLD films are amorphous. Thus upon annealing of the sputtered YSZ films it is energetically favored that the pre-existing grains grow by grain-boundary driven processes, consuming the adjacent amorphous parts. Whereas in the PLD case new seeds must be formed and isotropic grain growth with a different, significantly less pronounced texture is observed. It is possible to infer that orientation effects from the deposition affect the post-annealing step. The distinct initial situation obtained by two deposition techniques is most likely due to different growth regimes produced by the different energetic conditions. Typical energies in sputtering are on the order of a few eV whereas in PLD several ten to hundreds of eV are feasible along with a higher gas ionization.

4. Conclusions

The crystallization of 8 mol%-YSZ thin films deposited by low temperature RF-sputtering was investigated from room temperature to 1100 °C. The as-deposited thin films are characterized by a dense biphasic microstructure with crystallites' size from 5 to 10 nm building a columnar-like microstructure. In the temperature range from 800 to 1100 °C the crystallization process is accomplished within 40 h at the lower temperature resulting in a grain size of 25 nm with 0.5% microstrain, whereas at 1100 °C the grain size is 55 nm with 0.1% microstrain. The grain growth follows a stagnating-growth with an activation energy typical for grain-boundary diffusion of $E_a = 2.1$ eV. The crystallized samples, as revealed by X-ray diffraction and Raman spectroscopy, have a cubic symmetry preserved through the whole crystallization process.

8 mol%-YSZ thin films deposited by low temperature RF-sputtering present a stable microstructure with grain size below 100 nm resistant to thermally activated micro-structural coarsening and therefore are potentially useful as solid electrolytes in miniaturized power generation system with a reduced operating temperature.

Acknowledgements

Dieter Stender is heartily thanked for introduction to Raman spectroscopy measurements and Anja Weber for SEM images. JLM Rupp acknowledges the Swiss National Foundation for the advanced fellowship PA00P2-134153. L.J.G. acknowledges the cooperation with Prof. K. Sasaki and support from I2CNER project of Kyushu University, (J).

The project is part of the program 'Nanocrystalline ceramic thin films without sintering' (NANCER) funded by the Competence Center of Material Science and Technologies (CCMX) of the ETH board, Switzerland.

References

- [1] A. Evans, A. Bieberle-Hütter, H. Galinski, J.L.M. Rupp, T. Ryll, B. Scherrer, R. Tölke, L.J. Gauckler, *Monatsh. Chem. - Chem. Mon.* 140 (2009) 975–983.
- [2] A. Evans, A. Bieberle-Hütter, J.L. Rupp, L.J. Gauckler, *J. Power Sources* 194 (2009) 119–129.
- [3] B. Willing, M. Kohli, P. Muralt, O. Oehler, *Infrared Phys. Technol.* 39 (1998) 443–449.
- [4] R. Radhakrishnan, A. Virkar, S. Singhal, G. Dunham, O. Marina, *Sensors Actuators B Chem.* 105 (2005) 312–321.

- [5] D. Nikbin, Fuel Cell Rev. 3 (2006) 21–24.
- [6] A. Bieberle-Hütter, D. Beckel, A. Infortuna, U.P. Muecke, J.L. Rupp, L.J. Gauckler, S. Rey-Mermet, P. Muralt, N.R. Bieri, N. Hotz, M.J. Stutz, D. Poulikakos, P. Heeb, P. Müller, A. Bernard, R. Gmür, T. Hocker, J. Power Sources 177 (2008) 123–130.
- [7] J. Will, A. Mitterdorfer, C. Kleinogel, D. Perednis, L.J. Gauckler, Solid State Ionics 131 (2000) 79–96.
- [8] C.D. Baertsch, K.F. Jensen, J.L. Hertz, H.L. Tuller, S.T. Vengallatore, S.M. Spearing, M.A. Schmidt, J. Mater. Res. 19 (2004) 2604–2615.
- [9] J.L.M. Rupp, Solid State Ionics 207 (2012) 1–13.
- [10] D. Beckel, A. Bieberle-Hütter, A. Harvey, A. Infortuna, U. Muecke, M. Prestat, J. Rupp, L. Gauckler, J. Power Sources 173 (2007) 325–345.
- [11] M.S.R. Rao, C.P. D'Souza, P.R. Apte, R. Pinto, L.C. Gupta, S. Srinivas, A.K. Bhatnagar, J. Appl. Phys. 79 (1996) 940.
- [12] S. Heiroth, T. Lippert, A. Wokaun, M. Döbeli, J. Rupp, B. Scherrer, L. Gauckler, J. Eur. Ceram. Soc. 30 (2010) 489–495.
- [13] S. Heiroth, R. Frison, J.L. Rupp, T. Lippert, E.J. Barthazy Meier, E. Müller Gubler, M. Döbeli, K. Conder, A. Wokaun, L.J. Gauckler, Solid State Ionics 191 (2011) 12–23.
- [14] D. Perednis, O. Wilhelm, S. Pratsinis, L. Gauckler, Thin Solid Films 474 (2005) 84–95.
- [15] J.H. Joo, G.M. Choi, Solid State Ionics 177 (2006) 1053–1057.
- [16] I. Kosacki, T. Suzuki, V. Petrovsky, H.U. Anderson, Solid State Ionics 136–137 (2000) 1225–1233.
- [17] S. Heiroth, R. Ghisleni, T. Lippert, J. Michler, A. Wokaun, Acta Mater. 59 (2011) 2330–2340.
- [18] H. Tomaszewski, J. Haemers, N. De Roo, J. Denul, R. De Gryse, Thin Solid Films 293 (1997) 67–74.
- [19] D.J. Quinn, B. Wardle, S.M. Spearing, J. Mater. Res. 23 (2008) 609–618.
- [20] M. García-Sánchez, J. Peña, A. Ortiz, G. Santana, J. Fandiño, M. Bizarro, F. Cruz-Gandarilla, J. Alonso, Solid State Ionics 179 (2008) 243–249.
- [21] J. Maier, Z. Phys. Chem. 217 (2003) 415–436.
- [22] M. Greenberg, E. Wachtel, I. Lubomirsky, J. Fleig, J. Maier, Adv. Funct. Mater. 16 (2006) 48–52.
- [23] J.L. Rupp, L.J. Gauckler, Solid State Ionics 177 (2006) 2513–2518.
- [24] J.L.M. Rupp, B. Scherrer, A.S. Harvey, L.J. Gauckler, Adv. Funct. Mater. 19 (2009) 2790–2799.
- [25] J.L.M. Rupp, B. Scherrer, N. Schäuble, L.J. Gauckler, Adv. Funct. Mater. 20 (2010) 2807–2814.
- [26] B. Scherrer, S. Heiroth, R. Hafner, J. Martynczuk, A. Bieberle-Hütter, J.L.M. Rupp, L.J. Gauckler, Adv. Funct. Mater. 21 (2011) 3967–3975.
- [27] Z. Ji, J.M. Rigsbee, J. Mater. Sci. Lett. 20 (2001) 611–613.
- [28] S. Ben Amor, B. Rogier, G. Baud, M. Jacquet, M. Nardin, Mater. Sci. Eng. B 57 (1998) 28–39.
- [29] B.Y. Liaw, R.E. Rocheleau, Q.-H. Gao, Solid State Ionics 92 (1996) 85–89.
- [30] P. Gao, L.J. Meng, M.P.D. Santos, V. Teixeira, M. Andritschky, Thin Solid Films 377–378 (2000) 32–36.
- [31] Y.H. Wang, X.P. Li, Thin Solid Films 250 (1994) 132–134.
- [32] J.P. Riviere, S. Harel, P. Guerin, A. Straboni, Surf. Coat. Technol. 84 (1996) 470–475.
- [33] In: G.F. Vander Voort, F.J. Warmuth, S.M. Purdy, A. Szirmae (Eds.), Metallography - past, present, and future 75th anniversary volume, American Society for Testing and Materials, Philadelphia, PA, 1993.
- [34] FIT, <http://people.web.psi.ch/zolliker/public/>, ????
- [35] T.H. De Keijser, J.I. Langford, E.J. Mittemeijer, A.B.P. Vogels, J. Appl. Crystallogr. 15 (1982) 308–314.
- [36] J.I. Langford, A.J.C. Wilson, J. Appl. Crystallogr. 11 (1978) 102–113.
- [37] C.V. Thompson, Annu. Rev. Mater. Sci. 20 (1990) 245–268.
- [38] In: E.J. Mittemeijer, P. Scardi (Eds.), Diffraction Analysis of the Microstructure of Materials, Springer, Berlin, 2004.
- [39] I. Kosacki, C.M. Rouleau, P.F. Becher, J. Bentley, D.H. Lowndes, Solid State Ionics 176 (2005) 1319–1326.
- [40] P. Mengucci, G. Barucca, A. Caricato, A. Di Cristoforo, G. Leggieri, A. Luches, G. Majnina, Thin Solid Films 478 (2005) 125–131.
- [41] S. Sprio, S. Guicciardi, A. Bellosi, G. Pezzotti, Surf. Coat. Technol. 200 (2006) 4579–4585.
- [42] N. Sonnenberg, A.S. Longo, M.J. Cima, B.P. Chang, K.G. Ressler, P.C. McIntyre, Y.P. Liu, J. Appl. Phys. 74 (1993) 1027.
- [43] E. Fernandez Lopez, V. Sanchez Escribano, M. Panizza, M.M. Carnasciali, G. Busca, J. Mater. Chem. 11 (2001) 1891–1897.
- [44] F. Capel, M.A. Bañares, C. Moure, P. Durán, Mater. Lett. 38 (1999) 331–335.
- [45] C.H. Perry, D.W. Liu, R.P. Ingel, J. Am. Ceram. Soc. 68 (1985) (C-184–C-187).
- [46] A. Semjonow, E. Anastassakis, Physica A 201 (1993) 416–420.
- [47] H.G. Scott, J. Mater. Sci. 10 (1975) 1527–1535.
- [48] J. Suda, O. Kamishima, J. Kawamura, T. Hattori, T. Sato, J. Phys. Conf. Ser. 150 (2009) 052249.
- [49] J.L.M. Rupp, B. Scherrer, L.J. Gauckler, Phys. Chem. Chem. Phys. 12 (2010) 11114.
- [50] M. Kitajima, Crit. Rev. Solid State Mater. Sci. 22 (1997) 275.
- [51] J.R. McBride, K.C. Hass, B.D. Poindexter, W.H. Weber, J. Appl. Phys. 76 (1994) 2435.
- [52] J. Cai, Y.S. Raptis, E. Anastassakis, Appl. Phys. Lett. 62 (1993) 2781.
- [53] Z.D. Dohcevic-Mitrovic, M.J. Scepanovic, M.U. Grujic-Brojcin, Z.V. Popovic, S.B. Boskovic, B.M. Matovic, M.V. Zinkevich, F. Aldinger, Solid State Commun. 137 (2006) 387–390.
- [54] I.H. Campbell, P.M. Fauchet, Solid State Commun. 58 (1986) 739–741.
- [55] C.Y. Xu, P.X. Zhang, L. Yan, J. Raman Spectrosc. 32 (2001) 862–865.
- [56] A. Ghosh, A.K. Suri, M. Pandey, S. Thomas, T.R. Rama Mohan, B.T. Rao, Mater. Lett. 60 (2006) 1170–1173.
- [57] C.M. Phillippi, K.S. Mazdiyasi, J. Am. Ceram. Soc. 54 (1971) 254–258.
- [58] A. Ghosh, D.D. Upadhyaya, R. Prasad, J. Am. Ceram. Soc. 85 (2002) 2399–2403.
- [59] J.L. Shi, M.L. Ruan, T.S. Yen, Ceram. Int. 22 (1996) 137–142.
- [60] J.I. Langford, A. Boulif, J.P. Auffrédic, D. Louër, J. Appl. Crystallogr. 26 (1993) 22–33.
- [61] O. Masson, V. Rieux, R. Guinebrière, A. Dauger, Nanostruct. Mater. 7 (1996) 725–731.
- [62] J.L. Rupp, A. Infortuna, L.J. Gauckler, Acta Mater. 54 (2006) 1721–1730.
- [63] J.L. Rupp, C. Solenthaler, P. Gasser, U. Muecke, L.J. Gauckler, Acta Mater. 55 (2007) 3505–3512.
- [64] N.I. Karageorgakis, A. Heel, J.L.M. Rupp, M.H. Aguirre, T. Graule, L.J. Gauckler, Adv. Funct. Mater. 21 (2011) 532–539.
- [65] J. Dong, M.Z. Hu, E.A. Payzant, T.R. Armstrong, P.F. Becher, J. Nanosci. Nanotechnol. 2 (2002) 161–169.
- [66] B.P. Gorman, H.U. Anderson, J. Am. Ceram. Soc. 85 (2002) 981–985.
- [67] G. Theunissen, A. Winnubst, A. Burggraaf, J. Eur. Ceram. Soc. 11 (1993) 315–324.
- [68] Z. Shao, S.M. Haile, Nature 431 (2004) 170–173.
- [69] L. Shvindlerman, G. Gottstein, Int. J. Mater. Res. 4 (2004) 239.
- [70] M. Yan, R. Cannon, H. Bowen, Westview Press, 1976.
- [71] B. Scherrer, J. Martynczuk, H. Galinski, J.G. Grolig, S. Binder, A. Bieberle-Hütter, J.L.M. Rupp, M. Prestat, L.J. Gauckler, Adv. Funct. Mater. 22 (2012) 3509–3518.
- [72] S. Ramanathan, N. Soni, R. Prasad, J. Mater. Sci. Lett. 12 (1993).
- [73] C.-W. Kuo, Y.-H. Lee, I.-M. Hung, M.-C. Wang, S.-B. Wen, K.-Z. Fung, C.-J. Shih, J. Alloys Compd. 453 (2008) 470–475.
- [74] S. Ramanathan, R.V. Muralidharan, S.K. Roy, K. Padmanabha, K. Nayar, J. Am. Ceram. Soc. 78 (1995) 429–432.
- [75] M. Kilo, M.A. Taylor, C. Argiris, G. Borchardt, B. Lesage, S. Weber, S. Scherrer, H. Scherrer, M. Schroeder, M. Martin, J. Appl. Phys. 94 (2003) 7547.
- [76] H. Drings, U. Brossmann, H.-D. Carstanjen, Á. Szökefalvi-Nagy, C. Noll, H.-E. Schaefer, Phys. Status Solidi A 206 (2009) 54–58.
- [77] K.C. Lau, B.I. Dunlap, J. Phys. Condens. Matter 23 (2011) 035401.